Journal of Wind Engineering & Industrial Aerodynamics 250 (2024) 105762

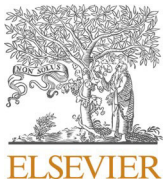

Contents lists available at ScienceDirect

Journal of Wind Engineering & Industrial Aerodynamics

journal homepage: www.elsevier.com/locate/jweia

Aerodynamic responses of tall buildings with cross-section modification through additive- and subtractive-based strategies

Wei-Ting Lu [a], Brian M. Phillips [a,*], Zhaoshuo Jiang [b]

[a] Department of Civil and Coastal Engineering, University of Florida, Gainesville, United States
[b] Department of Civil and Environmental Engineering, San Francisco State University, San Francisco, United States

ARTICLE INFO

Keywords:
Tall building
Aerodynamic strategy
Side protrusion
Corner modification
Wind tunnel testing
Structural response
Wind design

ABSTRACT

Aerodynamic modifications are recognized as an effective approach to mitigate wind responses for tall buildings. However, the relative effectiveness is highly dependent on (1) the benchmark (reference) model, and (2) the design wind speeds. In this study, a total of 21 cross-section modification models and 4 square benchmark models were tested using high-frequency force balance wind tunnel testing. The aerodynamic performance of the 21 models is assessed from both the perspective of additive-based side protrusions and subtractive-based corner recessions under a broad range of design wind speeds. The results indicate that the subtractive-based corner recession strategy has a higher chance to produce adverse responses at low wind speeds. On the contrary, promising aerodynamic performance under a broad range of wind speeds can be achieved via the additive-based side protrusion strategy using various protrusion ratios (PRs). Models SP-7-86, SP-14-71, and SP-21-29 are the ideal candidates for minor, medium, and major side protrusion strategies, respectively. The overturning moment (OTM) responses at the wind speeds of 53 m/s for the three models are reduced by 35%, 50%, and 48%, respectively.

List of acronyms and notations

B_a	The nominal building width from the perspective of additive design
B_F	The full-scale width of the benchmark model
B_s	The nominal building width from the perspective of subtractive design
$\overline{CMD}$	Mean along-wind base moment coefficient
$\overline{CML}$	Mean across-wind base moment coefficient
f_1	The building's full-scale fundamental natural frequency
f_R	Reduced frequency
g_B	The gust factor for the background component
g_R	The gust factor for the resonant component
H_F	Full-scale building height
M_B	Full-scale background OTM
M_R	Full-scale resonant OTM
$M_R(f)$	Full-scale resonant OTM
$\overline{M}$	Full-scale mean OTM
$\widehat{M}(f)$	Full-scale peak OTM
U_F	The full-scale wind speed at the rooftop
σ_{CMD}	Standard deviation along-wind base moment coefficient
σ_{CML}	Standard deviation across-wind base moment coefficient
σ_{M_HFFB}	The model-scale STD moment measured from HFFB testing
σ_M	Full-scale STD OTM
AE	Aeroelastic testing
B	The nominal width of the benchmark model
BLWT	Boundary layer wind tunnel
CFD	Computational fluids dynamics
CR	Corner recession
d	Protrusion length
DR	Depth ratio
f	The model-scale frequency under wind loading
H	The height of model
HFFB	High-frequency force balance
HOU	Houston
MIA	Miami
MRI	Mean recurrence interval
MWFRS	Main wind force resisting system
NY	New York
OTM	Overturning moment
PR	Protrusion ratio
PSD	Power spectral density
RECT	Rectangular
SF	San Francisco
SP	Side protrusion
SPM	Simultaneous pressure measurement
SQ	Square
STD	Standard deviation

(continued on next column)

(continued)

(continued on next page)

* Corresponding author.
E-mail address: brian.phillips@essie.ufl.edu (B.M. Phillips).

https://doi.org/10.1016/j.jweia.2024.105762
Received 10 October 2023; Received in revised form 6 May 2024; Accepted 6 May 2024
Available online 13 May 2024

(*continued*)

TFI	Turbulence flow instrumentation
U	The mean wind velocity at model top
UF	University of Florida
w	Protrusion width
WR	Width ratio
ξ	Damping ratio
ρ	Air density

1. Introduction

Under wind loading, structural responses (e.g., base moment, displacement, and acceleration) occur simultaneously in the along-wind and across-wind directions for tall buildings. The need to reduce across-wind responses for the main wind force resisting system (MWFRS) of tall buildings is well-recognized in the community of wind engineering. To mitigate wind responses, there are two approaches: (1) changing the structural properties, such as stiffness, mass, and damping (Griffis, 1993), and (2) modifying the external shape of the building, which is referred to as aerodynamic strategy. In general, the latter option is regarded as a more economical approach (Elshaer et al., 2017) and is the focus of this study.

Among various strategies listed in review papers on this topic (Xie, 2014; Mooneghi and Kargarmoakhar, 2016; Sharma et al., 2018; Jafari and Alipour, 2021), corner modification has been recognized as an effective solution, which has been successfully applied to real buildings, such as Taipei 101 and Mitsubishi Heavy Industries Yokohama Building. As reported in the literature (Irwin, 2009), the base moment of Taipei 101 was reduced by 25% using a double-corner recession strategy. Popular corner geometries are presented in Fig. 1, including rounded, chamfered, and recessed. Table 1 provides an overview of academic research on tall buildings with various corner modification strategies using wind tunnel testing and numerical simulation, including research approach, benchmark model, aerodynamic strategy, modification ratio, wind direction, and building height.

For the corner modification strategies, the modification ratio (defined as d/B_s, see Fig. 1) is a critical design parameter to influence the aerodynamic performance. As can be seen from Table 1, a modification of 3%–25% is considered a reasonable range. In general, a 10% corner modification ratio is regarded as a sweet spot to ensure the effectiveness with minor changes in the corner geometries (Xie, 2014; Mooneghi and Kargarmoakhar, 2016; Sharma et al., 2018; Irwin, 2009; Thordal et al., 2020).

Since structural responses of tall buildings under wind loading are dominated by the fluctuating component of the response in the across-wind direction (Griffis, 1993; Gu and Quan (2004); Gu and Quan (2004); Lu et al., 2023), the effectiveness of an aerodynamic strategy can be assessed using the power spectral density (PSD) of the base across-wind moment as compared to a benchmark model. An effective strategy will (1) reduce the PSD magnitude and/or (2) favorably shift (or maintain) the dominant frequency caused by vortex shedding. As indicated in the literature (Kwok et al., 1988; Miyashita et al., 1993; Tamura and Miyagi, 1999; Tanaka et al., 2012; Li et al., 2018), the corner modification is very effective to suppress the peak value of PSD. In comparison with a square benchmark model, however, the dominant frequency can be increased (Kwok et al., 1988; Li et al., 2020), which can result in adverse effects under low wind speeds (Lu et al., 2023).

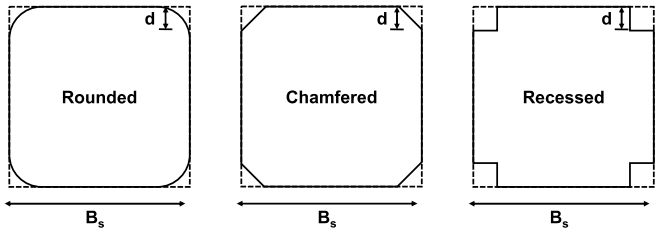

Fig. 1. Plan view of various corner modification strategies.

In addition to the reference benchmark model and design wind speed, the definition of the design space is a critical step in any aerodynamic strategy study. Because corner modifications affect the floor area, some studies preserve building volume by increasing the building height (Tse et al., 2009, 2021) or expanding the building footprint (Tanaka et al., 2012; Zheng et al., 2018). Constraints on the footprint (e.g., in urban areas) and height (e.g., flight safety or city regulation) may disallow this constant volume approach to normalize design alternatives. For most studies listed in Table 1, the height is fixed and the footprint of the benchmark model is taken as upper bound of the design space. As illustrated in Fig. 1, this means that both the building volume and floor area are reduced by applying the corner modification strategy, which is referred to herein as a subtractive-based design. Note that the design is only controlled by a single parameter, the corner modification ratio. A corner modification strategy with more than one design parameter to enrich the design space would be beneficial for designers to find a balance between the loss of floor area and the mitigation of wind response.

In addition to subtracting from a benchmark model, an additive-based side protrusion strategy was demonstrated effective by Lu et al. (2023). The idea of the strategy is to add the shaded areas (see B-W in Fig. 2) on the sides of the original square benchmark footprint, within an allowable larger footprint. It is worth mentioning that the protruding geometries can be integrated into the building volume or added as non-structural façade features (Liu et al., 2021, 2023a, 2023b; Hui et al., 2022).

Fig. 2 shows PSD curves for a square benchmark model (B-B), a subtractive-based corner recession model (S-B), and an additive-based side protrusion model (B-W) from high-frequency force balance (HFFB) tests. Detailed description of the models can be found in Lu et al. (2023). For S-B, although the peak PSD is significantly reduced, the responses over the reduced frequencies of 0.12–0.16 are larger than that of the benchmark model. The larger PSD responses over the reduced frequencies of 0.12–0.16 is corresponding to a 20% amplification of roof acceleration and drift at the full-scale wind speeds of 33 m/s to 44 m/s (Lu et al., 2023). Note that the similar adverse effects of corner recession strategy at low wind speeds was also pointed out in Tang et al. (2023). Although the amplification of PSD responses at high reduced frequencies for S-B is clear from Fig. 2, a more comprehensive investigation with various dimensions is needed to confirm this shorcoming of the subtractive-based corner recession strategy in real-world applications.

On the contrary, the adverse effect disappears for B-W, which reduces the PSD magnitude without a large shift in the response frequency. In addition, additive-based approaches preserve integrity of the original floor geometry, a promising feature for owners. For the side protrusion strategy, it is intuitive that the width and depth of the protrusion are critical design parameters for tall buildings. However, it is not clear about the influence of the two parameters on the aerodynamic performance of tall buildings under various wind speeds.

Although there are a lot of research using parametric studies (as listed in Table 1) and shape optimization techniques (Bernardini et al., 2015; Elshaer et al., 2017; Ding and Kareem, 2018; Elshaer and Bitsuamlak, 2018; Paul and Dalui, 2021; Lu et al., 2023b) on the topic of aerodynamic strategies for tall buildings, there are still some research gaps remaining. First, the effectiveness of aerodynamic strategies examined through various benchmark models has not been investigated. Second, a cross-section modification strategy with more than one geometric parameter has not been parametrically explored. Third, the effects of angles of attack and design wind speeds are often overlooked for aerodynamic studies. Note that the relationships or dependencies between the aspects mentioned above may not be easy to investigate through the shape optimization technique.

To fill the gaps, this study systematically investigates the effects of additive- and subtractive-based cross-section modification strategies for

Table 1
Overview of studies on corner modification for tall buildings.

Reference	Research approach	Benchmark	Aerodynamic strategy	Modification ratio	Building height	Length scale
Kwok et al. (1988)	AE	RECT (subtractive)	Chamfered	11%	180 m	1:400
Miyashita et al. (1993)	HFFB	SQ (subtractive)	Chamfered, Recessed	10%	300 m	1:380
Kawai (1998)	AE	SQ and RECT (subtractive)	Rounded, Chamfered, Recessed	3%–25%	300 m	1:600
Tamura and Miyagi (1999)	HFFB	SQ (subtractive)	Rounded, Chamfered	17%	–	–
Gu and Quan (2004)	HFFB	SQ (subtractive)	Chamfered, Recessed	5%, 10%, and 20%	300 m	1:500
Tse et al. (2009)	HFFB	SQ (same building volume)	Chamfered, Recessed	6%–27%	240 m–280 m	1:400
Tanaka et al. (2012)	HFFB and SPM	SQ (same building volume)	Chamfered, Recessed	10%	400 m	1:1000
Carassale et al. (2014)	HFFB and SPM	SQ (subtractive)	Rounded	7% and 13%	–	–
Alminhana et al. (2018)	SPM	RECT (subtractive)	Chamfered, Recessed	16%	180 m	1:400
Cao and Tamura (2018)	CFD	SQ (subtractive)	Rounded	17%	–	–
Li et al. (2018)	SPM	SQ (subtractive)	Rounded, Chamfered, Recessed	10%	400 m	1:500
Zheng et al. (2018)	SPM	SQ (same building volume)	Chamfered, Recessed	10%	180 m	1:300
Li et al. (2020)	SPM	RECT (subtractive)	Chamfered	6%–24%	183 m	1:300
Thordal et al. (2020)	CFD	RECT (subtractive)	Rounded, Chamfered	16%	180 m	1:400
Tse et al. (2021)	SPM CFD	SQ (same building volume)	Recessed	6%–19%	240 m–280 m	1:400
Dong et al. (2022)	CFD	SQ (subtractive)	Chamfered	14%	–	–
Lu et al. (2023)	HFFB	SQ (subtractive)	Recessed	14%	300 m	1:750
Tang et al. (2023)	AE	SQ (subtractive)	Recessed	10%	1000 m	1:1000

AE: aeroelastic testing, CFD: computational fluids dynamics, HFFB: high-frequency force balance, SPM: simultaneous pressure measurement, SQ: square footprint, RECT: rectangular footprint. Modification ratio is defined as the modification length (d) divided by the width of SQ building or square root of the long and short sides of RECT building.

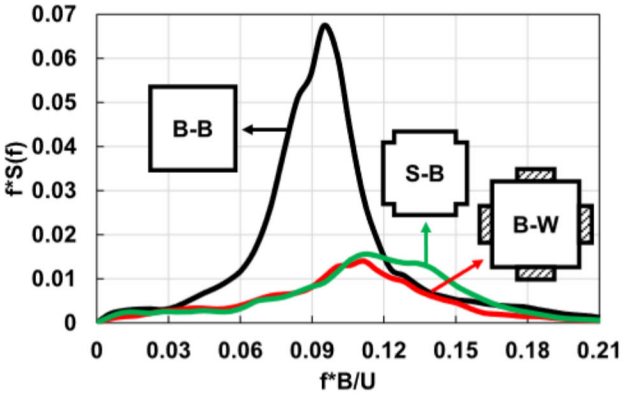

Fig. 2. PSD responses for square model (B-B), corner recession model (S-B), and side protrusion model (B-W) (Lu et al., 2023).

high-rise buildings under various design wind speeds. A total of 21 cross-section modification models and 4 square benchmark models were created. High-frequency force balance (HFFB) wind tunnel testing was carried out considering a full range of angles of attack. The peak OTM, considering the time and frequency domain results, is used to assess the aerodynamic performance of each model. First, the 21 modification models with various protrusion lengths and widths are assessed through the perspective of additive-based side protrusion strategy using a same square benchmark model. Second, the same modification models are evaluated from the standpoint of subtractive-based corner recession strategy via various square benchmark models. The results are expected to be useful information for wind engineers when it comes to various scenarios in real-world applications.

This paper is organized as follows: Section 2 introduces the detail of the 25 models. Section 3 describes the wind tunnel testing procedure and evaluation approach. The aerodynamic performance of each model is evaluated in Section 4, followed by the conclusions in Section 5.

2. Model description

In this study, all models are doubly symmetric and prismatic with a constant height of 300 m in full-scale. In wind tunnel testing, the height was 40 cm using a length scale of 1:750. Fig. 3 (a) illustrates the concept of additive-based side protrusion strategy with 2 design variables (w and d) on the sides of the square benchmark model with the nominal width of B_a. The same cross-section can be realized by subtractive design from the square benchmark model with the nominal width of B_s, as plotted in Fig. 3 (b).

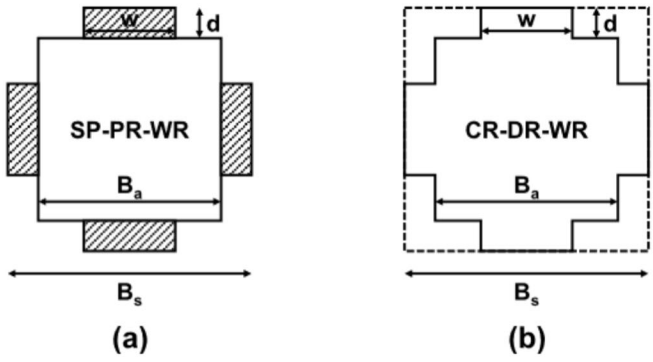

Fig. 3. Illustration graphs for (a) additive-based side protrusion strategy and (b) subtractive-based corner recession strategies.

As discussed in the Introduction, the performances of aerodynamic modification strategies are often compared to a benchmark model. Because this paper explores the perspectives of additive and subtractive design, several benchmark models are needed. Four square benchmark models ranging from 70 mm to 100 mm in width (see Fig. 4) were tested along with the modification models. The square models are designated by SQ followed by the width of the model. For example, SQ70 represents a square section of 70 mm × 70 mm. The plan views of the 21 cross-section modification models are plotted in Fig. 5. The parametric approach for both strategies is described below.

2.1. Additive aerodynamic strategy

For additive design, the 21 aerodynamic modification models are designated by SP-PR-WR. SP denotes the side protrusion (additive) strategy. PR and WR are protrusion ratio and width ratio, respectively. As shown in Fig. 5, the grey areas represent what makes each model unique while the white area is the underlying benchmark model dimensions (SQ70). PR and WR are the two parameters for the side protrusion strategy. PR is defined as:

$$PR = \frac{d}{B_a} \tag{1}$$

where d is the protrusion length, B_a is the nominal building width from the perspective of additive design (see Fig. 3 (a)). WR is defined as:

$$WR = \frac{w}{B_a} = \frac{w}{B_s * (1 - 2 * DR)} \tag{2}$$

where w is the protrusion width, B_s and DR are the parameters for subtractive design, which will be discussed next.

SQ70 is taken as the benchmark model to evaluate the aerodynamic performance of the additive-based side protrusion strategy. A total of 7 WRs, ranging from 14% to 100%, are investigated. A total of 3 PRs, which are 7%, 14%, and 21%, are selected to represent minor, medium, and major protrusion on the sides of the benchmark model. SP-7, SP-14, and SP-21 models refer to the first, second, and third columns of Fig. 5. The detailed dimensions for the 21 models are listed in Table 2.

2.2. Subtractive aerodynamic strategy

The same 21 models can be realized from the perspective of a subtractive strategy (See Fig. 5). For subtractive strategy, the model is designated by CR-DR-WR. CR denotes the revised corner recession (subtractive) strategy. The term "revised" refers to the two parameters used in what is normally a one parameter strategy. The two variables w and d create a rich design space for exploration of the subtractive-based strategy.

As shown in Fig. 3 (b), the model is recessed from the original benchmark model indicated in dash lines. DR is the depth ratio, which can be expressed as:

$$DR = \frac{d}{B_s} \tag{3}$$

where B_s is the nominal building width from the perspective of subtractive design. d is depth recessed from B_s. Note that DR is also known as the modification ratio (as discussed in the Introduction) of the traditional single-corner recession strategy. For the revised corner recession strategy, it is practical to select the DR first. As a result, the WR will be a function of DR as expressed in Equation (2).

The name for the revised corner recession (subtractive) strategy of each model is labeled in the parentheses in Fig. 5 and Table 2. The 7 WRs remain the same as the side protrusion (additive) strategy. The three DRs are 6% (minor), 11% (medium), and 15% (major), respectively. CR-6, CR-11, and CR-15 models refer to the first, second, and third columns of Fig. 5. The corresponding benchmark models for the three columns of

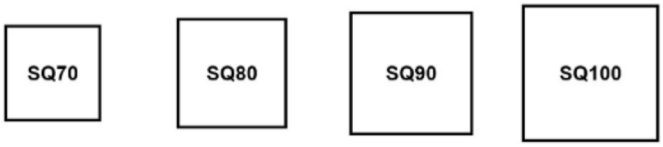

Fig. 4. Various SQ models.

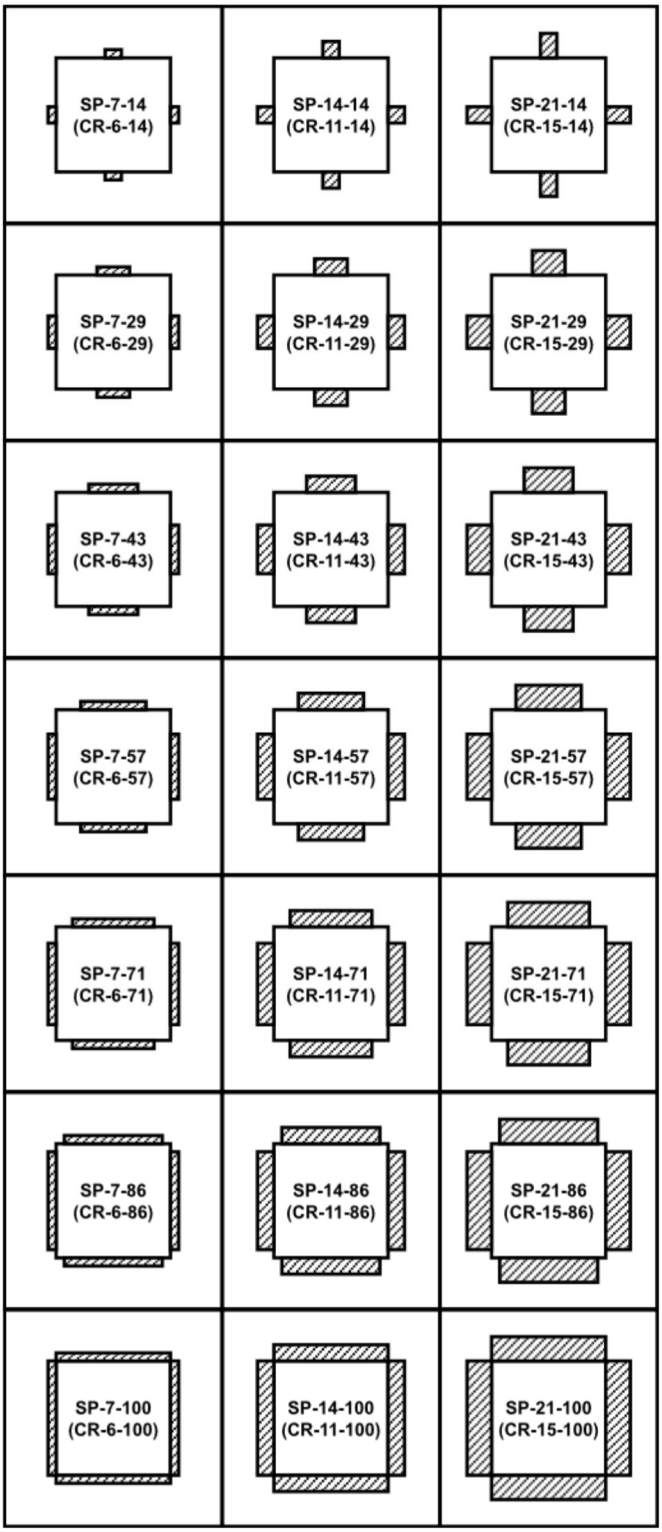

Fig. 5. Plan view of cross-section modification models.

Table 2
Dimensions of cross-section modification models (unit: mm).

Model	B_a	B_s	d	w	Model	B_a	B_s	d	w	Model	B_a	B_s	d	w
SP-7-14 (CR-6-14)	70	80	5	10	SP-14-14 (CR-11-14)	70	90	10	10	SP-21-14 (CR-15-14)	70	100	15	10
SP-7-29 (CR-6-29)	70	80	5	20	SP-14-29 (CR-11-29)	70	90	10	20	SP-21-29 (CR-15-29)	70	100	15	20
SP-7-43 (CR-6-43)	70	80	5	30	SP-14-43 (CR-11-43)	70	90	10	30	SP-21-43 (CR-15-43)	70	100	15	30
SP-7-57 (CR-6-57)	70	80	5	40	SP-14-57 (CR-11-57)	70	90	10	40	SP-21-57 (CR-15-57)	70	100	15	40
SP-7-71 (CR-6-71)	70	80	5	50	SP-14-71 (CR-11-71)	70	90	10	50	SP-21-71 (CR-15-71)	70	100	15	50
SP-7-86 (CR-6-86)	70	80	5	60	SP-14-86 (CR-11-86)	70	90	10	60	SP-21-86 (CR-15-86)	70	100	15	60
SP-7-100 (CR-6-100)	70	80	5	70	SP-14-100 (CR-11-100)	70	90	10	70	SP-21-100 (CR-15-100)	70	100	15	70

subtractive models are SQ80, SQ90, and SQ100, respectively. A WR of 100% (w = B_a) represents a traditional single-corner recession strategy with a defined DR. For example, CR-6-100, CR-11-100, and CR-15-100 are the three single-corner recession models. If the WR is $\frac{1-4*DR}{1-2*DR}$, a double corner recession strategy, such as Taipei 101, can be realized, which are CR-6-86, CR-11-71, and CR-15-57 in this study.

3. Experimental method and evaluation approach

3.1. HFFB testing setup

High-frequency force balance (HFFB) wind tunnel experiments were carried out in the boundary layer wind tunnel (BLWT) at the University of Florida (UF), which are presented in Fig. 6. The length of the BLWT is 38 m with a cross-section of 3 m in height and 6 m in width. The Terraformer (Catarelli et al., 2020a, 2020b) was used to simulate a suburban terrain condition with power-law index of 0.22. A terrain extension sheet was placed in between the Terraformer and the test section to maintain the flow condition up to the model. The mean wind speed and turbulence intensity along the height are shown in Fig. 7 (a). The mean wind speed at model top (40 cm) was 9.8 m/s. Based on the width of SQ70 (the smallest model in this study), the Reynolds number was 4.5×10^4, which was sufficiently higher than the minimum requirement of 1.1×10^4 (ASCE 49-21, 2021). The PSD of the velocity measured at the model height without the model in place is shown Fig. 7 (b). Since all models are doubly symmetric, the aerodynamic behavior of each model was tested under 10 angles of attack ranging from 0° to 45°, achieved via an automatic 1-m diameter turntable. Time series data were recorded for 1 min at each angle of attack at 2000 Hz using a six-axis load cell (ATI Industrial Automation, Delta model). A Turbulence Flow Instrumentation (TFI) cobra probe was placed 50 cm offset from the center of the model in the across-wind direction to record the reference wind speed at model top during wind tunnel testing.

3.2. Post-processing method

Before analyzing the data, it is necessary to determine the cutoff frequency of a low-pass filter used to process the measurements. Ideally, the cutoff frequency is larger than the upper bound of the frequencies of interest and smaller than the fundamental frequency of the physical model so that a wide range of frequency domain results can be discussed without the influence of the resonant responses from the physical model. In this study, the filter cutoff frequency and the model-scale fundamental frequency are 30 Hz and 50 Hz, respectively. Note that the first blade passage frequency of the wind tunnel is 113 Hz, well above the filter cutoff frequency. The aerodynamic responses are analyzed in three categories: (1) time domain response, (2) frequency domain response, and (3) structural response under different design wind speeds. For Category (1) and (2), the responses are divided into along-wind and across-wind directions (relative to the wind tunnel direction). Each direction has 10 angles of attack. The envelope responses of the time and frequency domain results across the 10 angles of attack are used to generate structural responses (i.e., Category (3)) in along-wind and across-wind directions. The detailed analysis procedure can be found in Lu et al. (2023). A brief description is presented below.

In the time domain, four non-dimensional base moment coefficients from different angles of attack are calculated, including mean along-wind ($\overline{CMD}$), mean across-wind ($\overline{CML}$), standard deviation (STD) along-wind (σ_{CMD}), and STD across-wind (σ_{CML}). To obtain the non-dimensional coefficients, statistics are calculated from time series data and normalized by $\frac{1}{2}\rho U^2 BH^2$, where ρ is the air density, U is the mean wind velocity at the model top (9.8 m/s), B is the nominal width of the benchmark model, H is the height of the model (0.4 m).

In the frequency domain, the PSD ($f * S(F)$) at various reduced frequencies are generated for different angles of attack in both along-wind and across-wind directions. The reduced frequency f_R is:

$$f_R = \frac{f * B}{U} = \frac{f_1 * B_F}{U_F} \tag{4}$$

where f is the model-scale frequency, f_1 is the building's full-scale fundamental natural frequency, which is assumed to be 0.1 Hz, B_F is the full-scale width of the benchmark model. U_F is the full-scale wind speed at the rooftop, which can be calculated based on f.

To estimate the fundamental frequency, there are different empirical formulas available in literature. For example, Ellis (1980) proposed a formula of 47/ H_F based on the field data of 163 buildings. Tamura (2012) also suggested different equations for different building types under various hazard levels. In addition to aerodynamic strategies, as mentioned in the Introduction, changing the fundamental frequency is also a solution that designers can use to mitigate wind responses for tall buildings (Griffis, 1993). The intention of using a lower fundamental frequency (0.1 Hz) than the empirical formula (e.g., 47/300m = 0.16

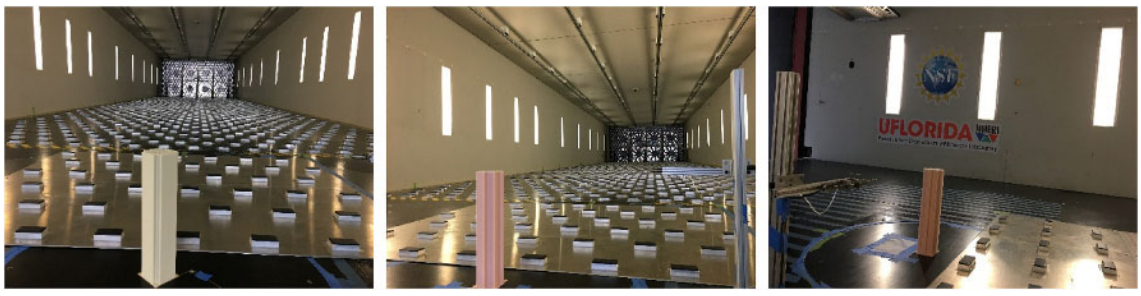

Fig. 6. Photographs of HFFB testing in the UF BLWT.

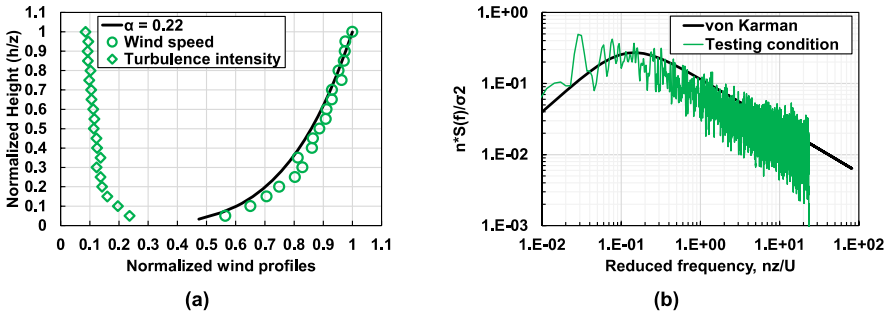

Fig. 7. BLWT approach flow conditions: (a) normalized wind speed and turbulence intensity; and (b) PSD responses at model height (z = 40 cm).

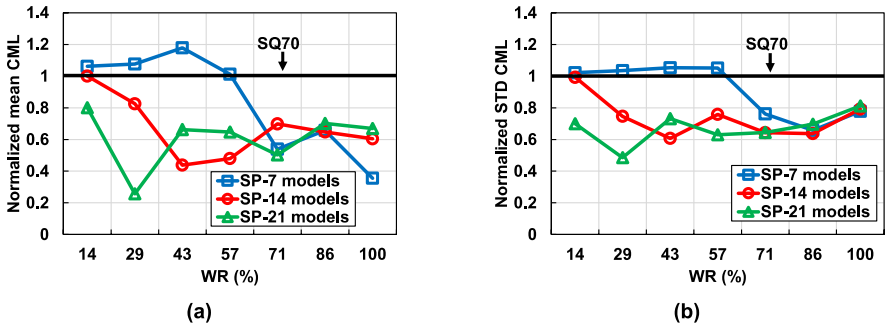

Fig. 8. The largest base moment coefficients enveloped over all angles of attack: (a) $\overline{CML}$; and (b) σ_{CML}.

Hz) was to ensure the full-scale structural responses would be within an acceptable range over the wind speeds of 35 m/s to 80 m/s, which was demonstrated in Lu et al. (2023) for buildings applied aerodynamic strategies with the same height and similar footprints. By assuming the same fundamental frequency for all models under various wind speeds, the influence of aerodynamic strategies can be directly compared and discussed through normalized responses. In other words, the relative performance between different models is not influenced by the decision of the full-scale frequency, which might vary at various wind speeds (Tamura, 2012).

As the low-pass filter cutoff frequency is 30 Hz for this study, the upper bound of f_R that can be investigated in PSD responses (Figs. 9–12) is 0.21 (30 Hz * 0.07 m / 9.8 m/s, dominated by SQ70) and the corresponding U_F is 24.5 m/s (0.1 Hz * 52.5 m / 0.21). In structural responses (Figs. 13–16), the mean hourly wind speeds of 35 m/s to 85 m/s at the rooftop are used to compare the aerodynamic performance between different strategies. Note that the range of wind speeds discussed are all comfortably higher than the lowest useable wind speed of 24.5 m/s that is created by the low-pass filter.

For structural response, the full-scale peak base overturning moment (OTM) over a broad range of design wind speeds is calculated in along-wind and across wind directions. Based on the assumption of a Gaussian process, the peak OTM can be expressed as (Tschanz and Davenport, 1983; Zhou et al., 2003; Kwon et al., 2008):

$$\widehat{M}(f) = \overline{M} + \sqrt{M_B^2 + M_R^2(f)} \tag{5}$$

where $\widehat{M}(f)$ is the full-scale peak OTM, $\overline{M}$ and M_B are the full-scale mean and background OTM obtained from the time domain results, and M_R is the full-scale resonant OTM considering both the time domain and frequency domain results. Since (1) critical responses do not occur at the same angle of attack for different aerodynamic strategies (Lu et al., 2023) and (2) approach angles of attack can vary along the height in reality (Tse et al., 2016; Liu et al., 2019; Zhou et al., 2021; Tang et al., 2023; Yan et al., 2023; Yuan et al., 2023), $\overline{M}$, M_B, and M_R are the envelope responses over all angles of attack (0°–45°) for conservativeness. The full-scale mean and STD base moments can be generated based on the non-dimensional base moment coefficients multiplied by $\frac{1}{2}\rho U_F^2 B_F H_F^2$. The full-scale background OTM is:

$$M_B = g_B * \sigma_M \tag{6}$$

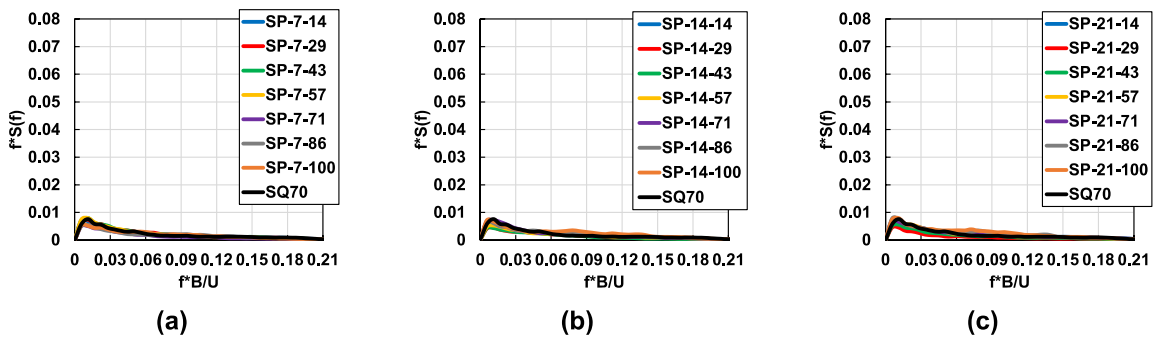

Fig. 9. Envelope of PSD responses in along-wind for cross-section modification models: (a) SP-7 models; (b) SP-14 models; and (c) SP-21 models.

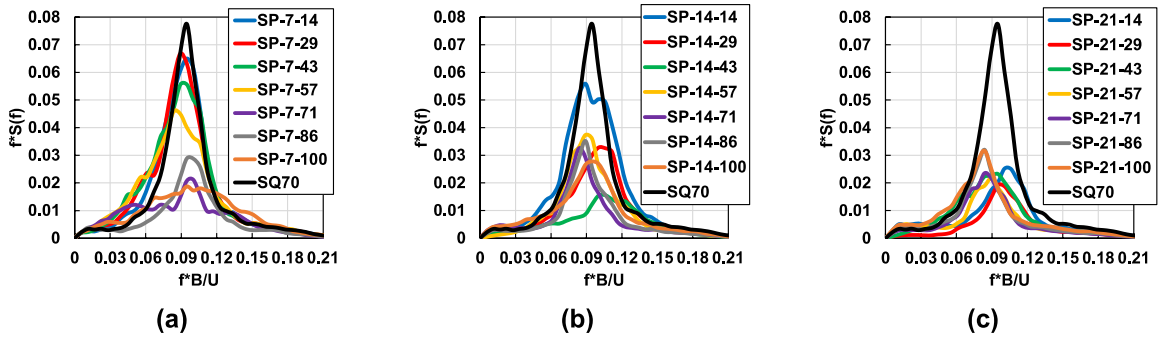

Fig. 10. Envelope of PSD responses in across-wind for cross-section modification models: (a) SP-7 models; (b) SP-14 models; and (c) SP-21 models.

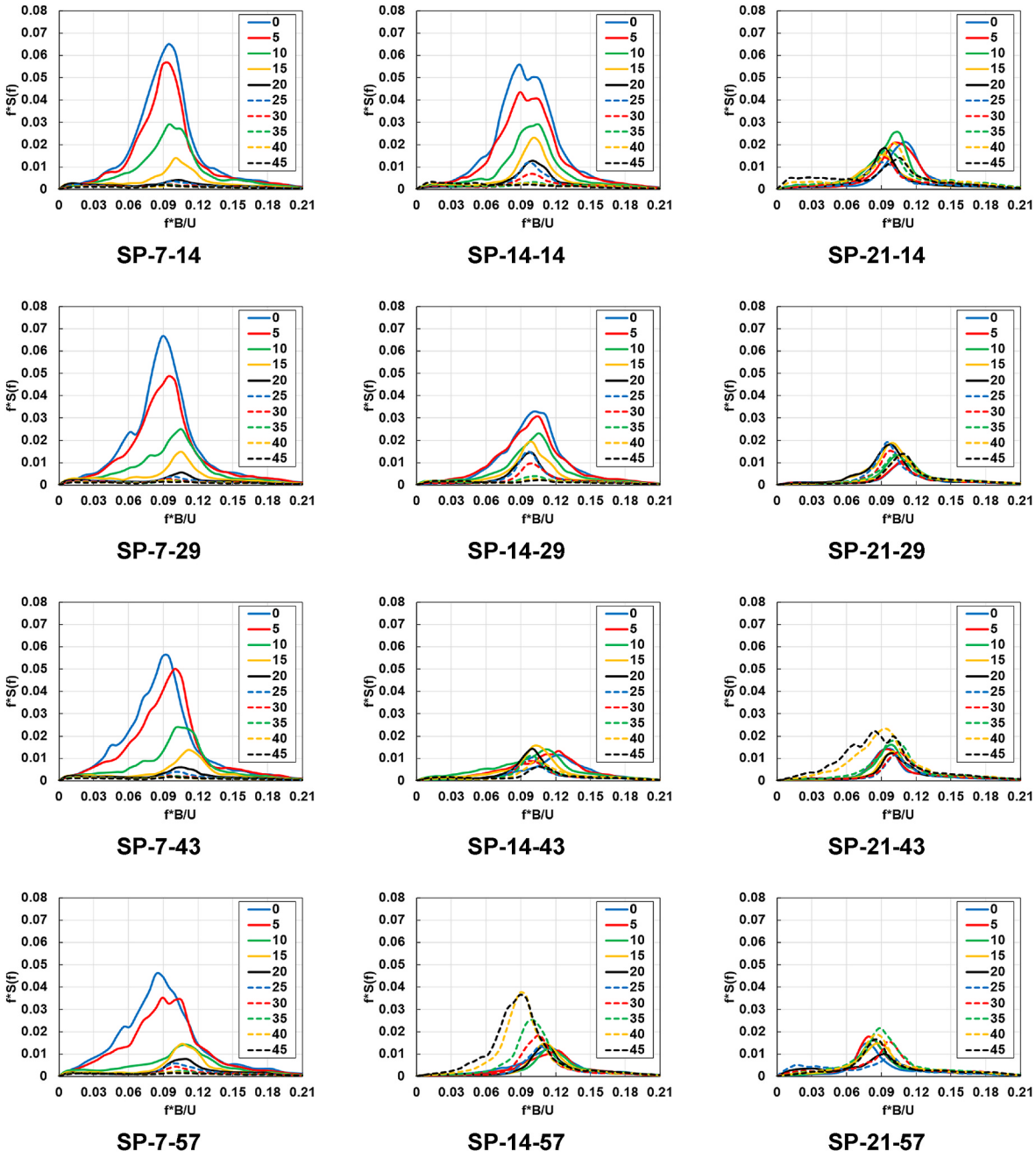

Fig. 11. Across-wind PSD responses under different angles of attack.

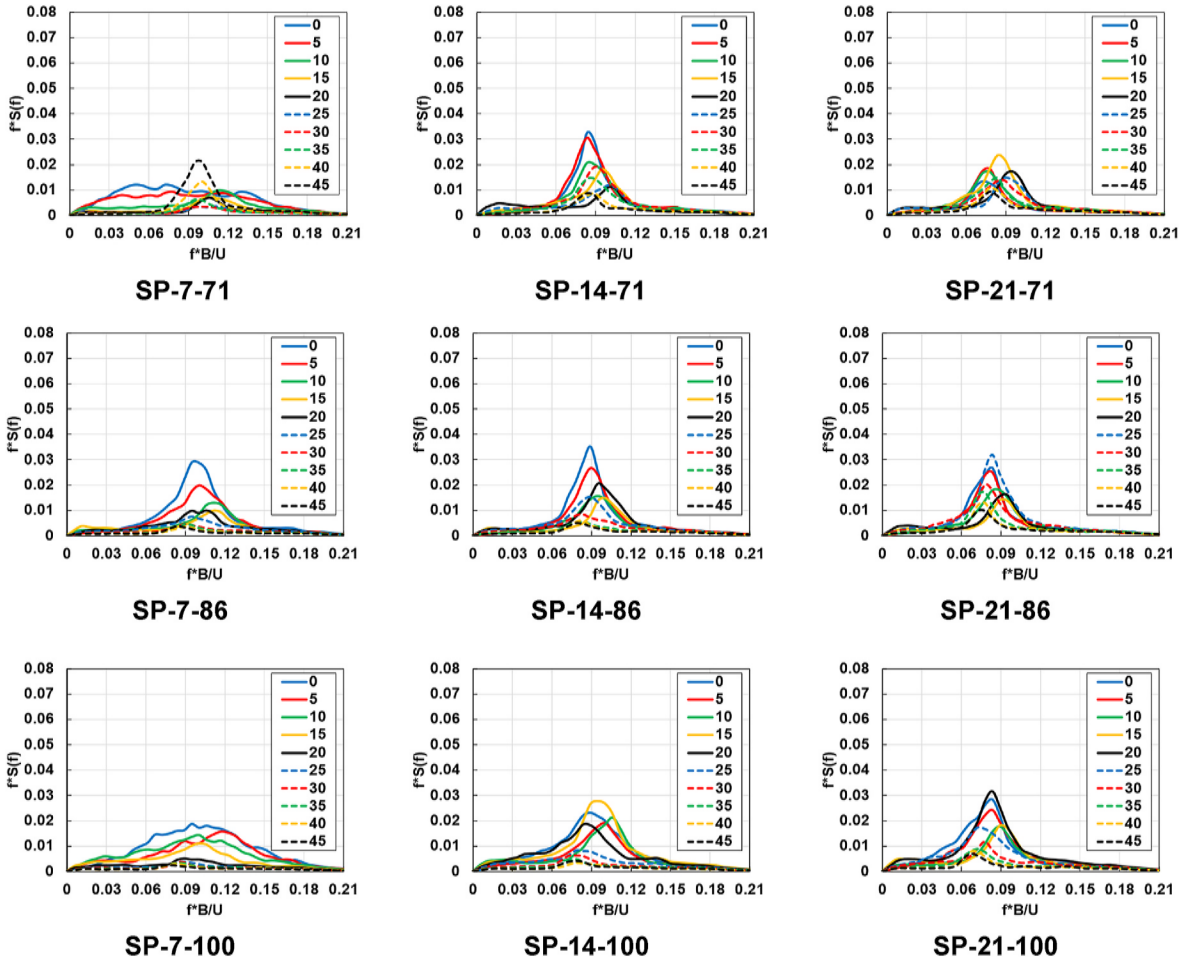

Fig. 11. (*continued*).

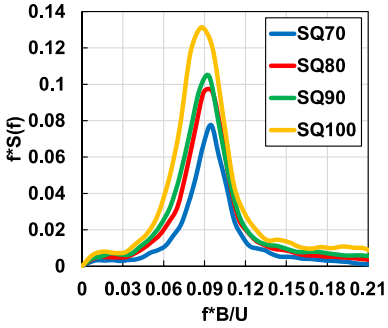

Fig. 12. Envelope of PSD responses in across-wind direction for various SQ models.

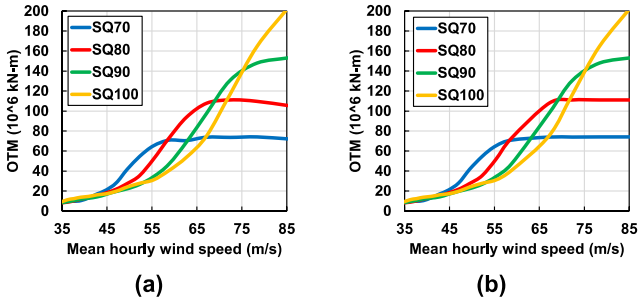

Fig. 13. Peak OTM for various SQ models: (a) direct response; and (b) cumulative largest response.

where g_B is the gust factor for the background component, and σ_M is the full-scale STD OTM, H_F is the full-scael building height. The full-scale resonant OTM is:

$$M_R(f) = g_R * \sigma_M * \sqrt{\frac{\pi}{4}\left(\frac{f * S(f)}{\sigma^2_{M_{HFFB}}}\right)\frac{1}{\xi}} \tag{7}$$

where g_R is the gust factor for the resonant component, σ_{M_HFFB} is the model-scale STD moment measured from HFFB testing, ξ is the damping ratio. $\frac{f*S(f)}{\sigma^2_{M_{HFFB}}}$ is the amplification factor for the resonant component, which dominates the peak OTM of high-rise buildings (Lu et al., 2023). The gust factor for the background and resonant OTM are selected as 3.5 (Tschanz and Davenport, 1983; Zhou et al., 2003; Kwon et al., 2008). The damping ratio is selected as 1% for all models.

4. Wind tunnel testing results

This section discusses the wind tunnel testing results for the 21 aerodynamic modification models. For simplicity, model names are all presented using the additive-based side protrusion strategy (SP-PR-WR). The corresponding names for the subtractive-based corner recession strategy (CR-DR-WR) can be found in Fig. 5. In the time domain (Section 4.1) and frequency domain (Section 4.2), a consistent nominal width of 7 cm (SQ70) was used for the 21 models to discuss the non-dimensional

base moment coefficients and the PSD responses at various reduced frequencies. The purpose of Section 4.1 and 4.2 is to present the relative performance between different modification models. For the full-scale OTM (Section 4.3), the 21 models are normalized by various square benchmark models to evaluate the relative performance from the perspectives of additive- and subtractive-based designs for the MWFRS.

4.1. Time domain results

Since the full-scale OTM is dominated by the across-wind direction (will be discussed in Section 4.2), only $\overline{CML}$ and σ_{CML} are analyzed here. Fig. 8 shows the largest $\overline{CML}$ and σ_{CML} enveloped over all angles of attack for SP-7, SP-14, and SP-21 models normalized by SQ70. It can be observed that the trends for $\overline{CML}$ and σ_{CML} between different models are similar but not identical. The relative performance between different models is discussed using the results of σ_{CML} since it affects both the background and resonant OTM components.

For SP-7 models (see Fig. 8 (b)), the σ_{CML} responses are larger than that of SQ70 for WRs of 14%–57%, suggesting the minor protrusion is not effective over the range of WRs. When WR is larger than 57%, the σ_{CML} is significantly decreased. SP-7-86 produces the smallest σ_{CML}, which is 0.66, among the SP-7 models. For medium protrusion (SP-14 models), the best performance is 0.61 occurred at SP-14-43. The normalized σ_{CML} responses vary in the range of 0.6–0.8 for WRs of 29%–100%. The larger effective range of WR suggests that both the PR and WR provide complementary effect to suppress the aerodynamic responses in the across-wind direction. For significant protrusion (SP-21 models), the WRs for 14%–100% are all effective to produce promising σ_{CML}. SP-21-29 produces the best σ_{CML}, which is 0.49, not only among the SP-21 models but the 21 aerodynamic modification models.

4.2. Frequency domain results

4.2.1. The envelope of PSD responses for aerodynamic modification models

The envelopes of PSD responses in the along-wind and across-wind for the aerodynamic modification models and SQ70 are presented in Figs. 9 and 10, respectively. Responses are enveloped over all angles of attack. As mentioned in Section 3, the range of interest for the mean hourly wind speeds is from 35 m/s to 85 m/s, which corresponds to the reduced frequencies of 0.06–0.15, respectively. In comparison with the magnitudes shown in Fig. 10, the negligible PSD responses in along-wind (Fig. 9) for the reduced frequencies of interest suggest that the MWFRS design for each model is dominated by the across-wind direction.

With respect to relative aerodynamic performance, the frequency domain results can be evaluated based on (1) the reduction of the PSD responses at various frequencies, and (2) the change of the dominant resonant frequency (or the Strouhal number) in comparison with a reference model. For the latter item, in general, the Strouhal number for a tall building with a square footprint under turbulent flow is around 0.1 (Tanaka et al., 2012; Moorjani et al., 2021). As shown in Fig. 10, the results of SQ70 agrees with the literature. In addition to the footprint of a model, the PSD responses and the corresponding Strouhal number are also influenced by flow conditions (Tamura and Miyagi, 1999). For example, the Strouhal number and the peak PSD of a square cylinder under two-dimensional flow are higher than that of three-dimensional flow. The bandwidth of PSD increases with the turbulent intensity.

For minor protrusion (SP-7 models, see Fig. 10 (a)), the peak PSD is significantly reduced for WRs of 71%–100%, which is consistent with the time domain results. For example, the peak PSD for SP-7-71 is decreased from 0.077 to 0.021, in comparison with SQ70. Regarding the reduction at different reduced frequencies, the responses for the models with a WR smaller than 57% are larger than that of SQ70 over low reduced frequencies (0.06–0.09), indicating the models are not effective to suppress structural responses at high wind speeds. On the contrary, the greater responses of SP-7-100 over higher reduced frequencies (0.12–0.15) suggest worse structural responses over low wind speeds. Among the SP-7 models, SP-7-71 and SP-7-86 are effective WRs to mitigate the resonant component under various wind speeds from the perspective of the additive-based aerodynamic strategy.

For medium protrusion (Fig. 10 (b)), when the WR is between 29% and 100%, the peak PSD can be significantly reduced. In line with the time domain results, SP-14-43 produces the best peak PSD, which decreased from 0.077 to 0.015. However, the PSD responses for SP-14-43 are slightly larger than that of SQ70 for reduced frequencies of 0.12–0.15, which also occurs in SP14-14 and SP-14-29. The larger bandwidth of SP-14-14 also leads to worse responses over low reduced frequencies (0.06–0.08). Due to the relatively limited reduction of peak PSD and wider PSD curve, SP-14-14 is not an ideal configuration to reduce the resonant component for tall buildings. For PR larger than 43%, the PSD responses are reduced over all the frequencies of interest in comparison with SQ70.

As shown in Fig. 10 (c), it can be observed that the resonant reduced frequencies are slightly decreased with a larger WR. This suggests that a wider WR is more effective to suppress the wind responses over low wind speeds for significant side protrusion strategy. The similar peak PSD responses for SP-21 models suggests the effectiveness of the significant protrusion to suppress the dynamic responses in the across-wind direction. With respect to the reduction over various frequencies, the PSD for SP-21-43 and SP-21-100 are slightly larger than that of SQ70 for reduced frequencies smaller than 0.08. Except for this, the responses for SP-21 models are all smaller than that of SQ70 over the reduced frequencies of interest. Among SP-21 models, SP-21-29 appears to be the best side protrusion configuration because of the narrow bandwidth of PSD curve in comparison with other models.

4.2.2. PSD responses for aerodynamic modification models under various angles of attack

Fig. 11 shows the PSD responses for the 21 aerodynamic modification models under various angles of attack. Note that the envelope responses discussed in Fig. 10 are the results extracted from Fig. 11. As reported by Lu et al. (2023), the PSD responses at different frequencies are all dominated by the angle of attack of 0° for the square model. In Fig. 11, it can be observed that (1) the peak PSD is not always dominated by the angle of attack of 0°, and (2) the PSD responses are dominated by various angles of attack at different reduced frequencies for the 21 aerodynamic modification models. The statements also apply to the traditional single-corner recession models with various DRs. For minor single corner recession (SP-7-100 or CR-6-100), the responses are dominated by the angle of attack of 0° at various frequencies due to the broad bandwidth of the PSD curve. The peak PSD responses are dominated by the angle of attack of 15° and 20° for SP-14-100 (CR-11-100) and SP-21-100 (CR-15-100), respectively. The results emphasize the necessity to consider various angles of attack when different aerodynamic strategies are considered to mitigate wind responses.

On the other hand, it can be observed that the trends for some models are significantly different from adjacent configurations. For example, the trends of PSD for SP-7-71 at various angles of attack are completely different from SP-7-57, SP-7-86, and SP-14-71. This also occurs to other models, such as SP-14-57 and SP-21-43. This shows that the aerodynamic behavior of tall buildings is indeed very sensitive to the change of PR and WR even though the parameters are continuous (discretely sampled) in the parametric study. One common behavior for SP-7-71, SP-14-57, and SP-21-43 is that the dominant angles of attack for the peak PSD are around 40°–45°, which is completely different from a square model.

4.2.3. The envelope of PSD responses for SQ models

Section 4.3 investigates the structural responses of aerodynamic modification models from different perspectives. To facilitate the investigation, the PSD responses for different widths of SQ models are

first discussed herein. Fig. 12 shows the envelope of PSD responses across all angles of attack for each SQ model. Note that the B used to normalize the PSD curve in the figure is equal to the width of the model. With respect to magnitude, the PSD responses, especially for the peak, are increased with model dimension, suggesting that the resonant component is proportional to the width of the building. The similar reduced dominant frequency for various SQ models confirms that the resonant wind speed will be increased with the building footprint. For the same length scale of 1:750, the full-scale building width (B_F) for SQ70, SQ80, SQ90, and SQ100 are 52.5 m, 60 m, 67.5m, and 75 m, respectively. Using the Strouhal number of 0.1 and the fundamental frequency of 0.1 Hz in Equation (4), the resonant full-scale wind speeds for the four models are 52.5 m/s, 60 m/s, 67.5 m/s, and 75 m/s, respectively. The various resonant wind speeds will lead to nonlinear relationship of aerodynamic responses between different SQ models when different wind speeds are considered, which will be discussed in the next subsection.

4.3. Structural responses

This subsection evaluates the structural responses for the 21 aerodynamic modification models under a broad range of wind speeds using the peak OTM. First, the responses between different dimensions of SQ models are presented. Second, the relative performance of each aerodynamic modification model is discussed from the perspective of additive-based (SP-PR-WR) and subtractive-based (CR-DR-WR) aerodynamic strategies. For the additive strategy perspective, the same benchmark model (SQ70) is used to evaluate the effectiveness of the 21 aerodynamic modification models. For the subtractive strategy perspective, the CR-6, CR-11, and CR-15 models are normalized by SQ80, SQ90, and SQ100, respectively.

4.3.1. SQ models

Fig. 13 shows the full-scale peak OTM of each SQ model over mean hourly wind speeds of 35 m/s to 85 m/s at the building top. Because of the variation of the PSD at different frequencies, the OTM responses do not linearly increase with wind speed.

As shown in Fig. 13 (a), the OTM significantly increases before reaching the resonant wind speed. Then, the response enters a plateau, resulting from (1) the increase of the velocity pressure ($\frac{1}{2}\rho U_F^2 B_F H_F^2$) from wind loading, and (2) the decrease of the PSD (on the left-hand side of resonant frequency, see Fig. 10) for the resonant component. On the plateau, the two inverse factors can slightly increase or decrease the OTM as wind speed increases. If the OTM is decreased, an unconservative design for MWFRS can occur. For example, the peak OTM for SQ80 is decreased from $111*10^6$ kN-m to $105*10^6$ kN-m for the wind speeds of 72 m/s to 85 m/s. If the design wind speed is 85 m/s, the OTM of $111*10^6$ kN-m should be used, instead of $105*10^6$ kN-m. To achieve a conservative design, the largest cumulative responses up to a design wind speed should be applied for the demand of MWFRS. The cumulative largest OTM responses at various wind speeds are presented in Fig. 13 (b). In comparison with Fig, 13 (a), the difference is that the responses for each model do not decrease as wind speed increases (see the results of SQ70 and SQ80).

Due to the variation of resonant wind speeds, it can be observed that a smaller SQ model will have a greater OTM in comparison with a larger counterpart under the excitation of low wind speeds, as shown in Fig. 13 (b). For example, the design demands of OTM for SQ70 are larger than that of SQ80 for wind speeds of 45–57 m/s. The nonlinear relationship between the building width and aerodynamic performance suggests that increasing the footprint (if possible) is also a feasible strategy to mitigate wind responses for tall buildings, especially for cities, such as San Francisco, with a lower design wind speed since there is no need to consider a higher wind speed beyond the design mean recurrence interval (MRI).

4.3.2. Aerodynamic modification models

The peak OTM versus design wind speed for SP-7 (CR-6), SP-14 (CR-11), and SP-21 (CR-15) models are presented in Fig. 14, Fig. 15, and Fig. 16, respectively. As a reminder, SP and CR are the same models from different perspectives. Each figure subplot presents: (a) the cumulative largest OTM, (b) the normalized OTM from the perspective of additive-based strategy, and (c) the normalized OTM from the perspective of subtractive-based strategy. Mean hourly design wind speeds at the rooftop for survivability (1700-year MRI (Category (3)), ASCE 7-22, 2022) at San Francisco (SF), New York (NY), Houston (HOU), and Miami (MIA) are labeled in subplot (a). The design wind speeds for the four cities are 42 m/s, 53 m/s, 62 m/s, and 77 m/s, respectively. These results will be discussed from the perspective of additive aerodynamic strategies in Section 4.3.2.1 and subtractive in Section 4.3.2.2.

4.3.2.1. Additive aerodynamic strategy. For minor protrusion (see Fig. 14 (b)), when the WR is smaller than 71%, the OTM is greater than that of SQ70 for most wind speeds. Thus, they (SP-7-14, SP-7-29, SP-7-43, and SP-7-57) are not considered as effective aerodynamic strategies for tall buildings. Although SP-7-71 and SP-7-100 can produce a promising performance for wind speeds higher than 55 m/s, the larger responses for wind speeds of 35 m/s to 45 m/s is not preferred for the survivability design of SF and can generate an issue of serviceability design for other cities (i.e., the mean hourly design wind speed for MIA at 10-year MRI is 38 m/s). As demonstrated in the literature (Lu et al., 2023), SQ70 cannot satisfy the criteria of serviceability (roof acceleration: 20 milli-g, ASCE, 2019) for wind speeds higher than 28 m/s. The performance for wind speeds lower than 55 m/s is taken as an important indicator to evaluate the aerodynamic strategies herein because it covers various design levels across multiple cities (i.e., in the absence of a particular case study). In Fig. 14 (b), overall, SP-7-86 is regarded as the most effective strategy among minor protrusion strategies (SP-7 models). In comparison with SQ70, the reduction of OTM for SP-7-86 at SF, NY, HOU, and MIA design wind speeds are 16%, 35%, 43%, and 42%, respectively.

For SP-14 models (see Fig. 15 (b)), SP-14-14 and SP-14-29 are not effective strategies due to the increase of OTM over low wind speeds, which resulted from the greater PSD over high reduced frequencies. Although SP-14-43 performs promising for wind speeds higher than 55 m/s, the responses are increased by 10% around a wind speed of 40 m/s. Also, SP-14-43 is not competitive for the design demands of SF and NY in comparison with other models. For medium protrusion, SP-14-71 and SP-14-86 are taken as the ideal options. In comparison with SQ70, the reduction of OTM for SP-14-71 at SF, NY, HOU, and MIA are 42%, 50%, 30%, and 25%, respectively. The results for SP-14-86 are 36%, 47%, 30%, and 30%, respectively.

Fig. 16 (b) shows the normalized OTM responses for the SP-21 models. Except for SP-21-14, the normalized OTM can be reduced by more than 20% under low wind speeds. For significant protrusion, SP-21-29 is selected as the most ideal option to mitigate the wind speed from 35 m/s to 85 m/s. The reduction of OTM for the model at SF, NY, HOU, and MIA are 33%, 48%, 56%, and 57%, respectively. Although the aerodynamic performance for the models with a WR larger than 21% (SP-21-43, SP-21-57, SP-21-71, SP-21-86, SP-21-100) are not as promising as SP-21-29 for wind speeds higher than 55 m/s, they are equally competitive if SF or NY are the upper bounds of design demands of survivability, implying ideal configurations vary with design wind speeds.

4.3.2.2. Subtractive aerodynamic strategy. Fig. 14 (c) shows the OTM responses for the CR-6 (SP-7) models normalized by SQ80. When the WR is smaller than 71%, the OTM responses are increased by more than 30% for wind speeds of 45 m/s to 55 m/s. The adverse effect is attributed to the lower resonant wind speeds for the CR-6 models in comparison with SQ80. For traditional single corner recession (CR-6-100/SP-7-100) and

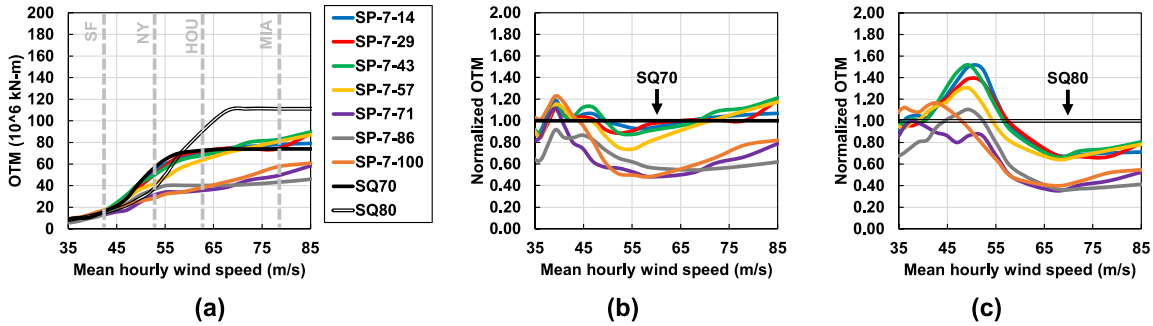

Fig. 14. Cumulative largest OTM for SP-7 (CR-6) models: (a) original response; (b) normalized by SQ70; and (c) normalized by SQ80.

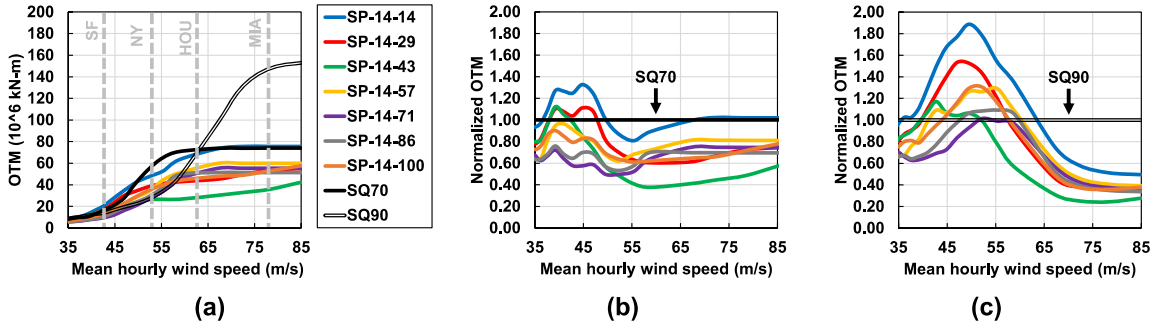

Fig. 15. Cumulative largest OTM for SP-14 (CR-11) models: (a) original response; (b) normalized by SQ70; and (c) normalized by SQ90.

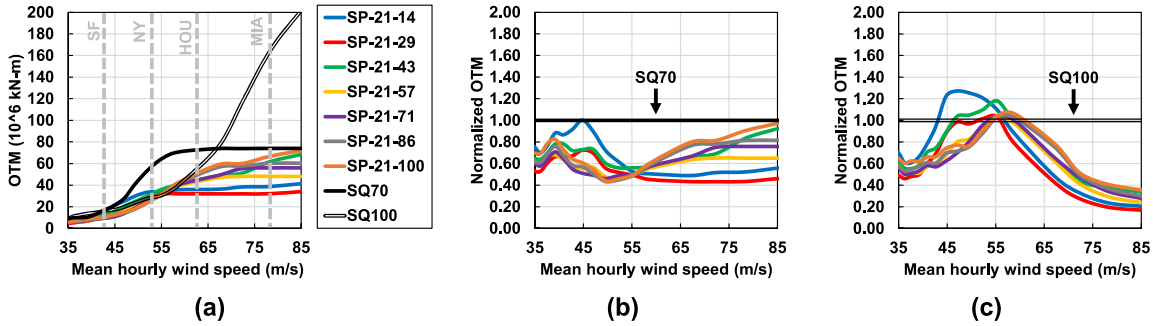

Fig. 16. Cumulative largest OTM for SP-21 (CR-15) models: (a) original response; (b) normalized by SQ70; and (c) normalized by SQ100.

double corner recession (CR-6-86/SP-7-86), the responses are also larger than SQ80 by more than 10% for wind speeds of 35 m/s to 55 m/s. Overall, CR-6-71/SP-7-71 is the optimal configuration for the subtractive-based corner recession strategy from SQ80. As expected, the optimal candidate is the not the same from the same group of models if a different benchmark model is used. The reductions of OTM for CR-6-71 at SF, NY, HOU, and MIA are 10%, 14%, 59%, and 55%, respectively.

For medium recession models (see Fig. 15 (c)), the adverse effect over low wind speeds is significant recessed from SQ90. In addition to the model with small WRs, the responses of CR-11-100/SP-14-100 are increased by 30% for wind speeds of 45 m/s to 55 m/s. The results indicate that (1) the importance of carefully selecting an appropriate WR for the cross-section modification strategy, and (2) the issue of the traditional single-corner recession strategy for tall buildings over low wind speeds. Among CR-11 models, CR-11-71/SP-14-71 performs the best, which is the well-cognized double-corner recession strategy applied to Taipei 101. The mitigation of OTM for CR-11-71 at SF, NY, HOU, and MIA is 31%, 0%, 23%, and 63%, respectively.

Fig. 16 (c) shows the OTM responses for CR-15 (SP-21) models normalized by SQ100. Although CR-15-14/SP-21-14 and CR-15-29/SP-21-29 produce promising responses for wind speeds higher than 55 m/s, the performance under low wind speeds is worse than that of the benchmark model. Again, the same model (CR-15-29/SP-21-29) has different relative performances from different perspectives of aerodynamic designs. For models with a WR larger than 43%, the responses are equally well for low wind and high wind speeds but are slightly larger (less than 5%) than that of SQ100 for wind speeds of 55 m/s to 60 m/s. For single corner recession (CR-15-100/SP-21-100), the reduction of OTM at SF, NY, HOU, and MIA is 33%, 10%, 8%, and 60%, respectively.

4.3.3. *Discussion*

As discussed in the Introduction, benchmark model, design wind speed, and design space are the factors need to consider when it comes to evaluate the effectiveness of any aerodynamic strategies. The aerodynamic behaviors of the 21 cross-section modification models were normalized by different benchmark models from the perspective of additive- and subtractive-based strategies under a broad range of design wind speeds. The normalized OTM responses show that the appropriate WRs do not occur on the boundaries (i.e., 0% or 100%) for both

strategies, which demonstrates the benefit to have this additional parameter to improve wind responses of tall buildings (i.e., beyond single corner recession).

Since different benchmark models were used for the subtractive-based design (CR-6, CR-11, and CR-15 models), the relative performance of OTM at different wind speeds is not expected to apply to a same benchmark model with various DRs. However, the trends suggest that the normalized OTM for most of the CR models, including the traditional single corner recession, are larger than their benchmark models over low wind speeds, confirming the downside of the subtractive-based modification strategy in real-world applications. For the additive design strategy, in comparison with SQ70, similar promising performance can be achieved via various combinations of PR and WR under different wind speeds.

The need to reduce wind responses for tall buildings is well-recognized in the community of wind engineering. The situation that a building performs worse after applying an aerodynamic strategy should be avoided. Combining the trends discussed above, the additive-based strategy is a more promising strategy than that of the subtractive-based strategy from the perspective of a common benchmark model (concisely illustrated in Fig. 2), which provides useful information of applying cross-section modification for tall buildings in the industry.

In addition to aerodynamic performance, there might be other considerations, such as operation space or footprint constraints, that need to take into consideration. Other than using structural components, it is worth mentioning that additive strategies (e.g., side protrusion), especially for minor protrusions, can be achieved via nonstructural components, such as mullions (Stathopoulos and Zhu, 1990), dynamic façade (Ding and Kareem, 2020), double-skin façades (Hu et al., 2017, 2019; Hou et al., 2023; Skvorc and Hozmar, 2023), or curtain walls (Quan et al., 2016). With these techniques and knowledge, structural engineers have more options to achieve a balance between different design objectives for high-rise buildings.

5. Conclusions

This paper investigates the aerodynamic performance of the main wind force resisting system (MWFRS) for tall buildings with different footprints and cross-sections. A total of 21 cross-section modification models are evaluated from the perspective of additive-based side protrusion and subtractive-based corner recession strategies using different sizes of square (SQ) benchmark models. The modification models are controlled by two parameters, width ratio (WR) and protrusion ratio (PR). The latter parameter is also called the depth ratio (DR) in the subtractive-based strategy. High-frequency force balance (HFFB) wind tunnel testing was carried out to examine the aerodynamic behavior of each model under different angles of attack. The base moment coefficients in the time domain and power spectral density (PSD) responses in the frequency domain are used to generate the peak overturning moment (OTM) under wind speeds of 35 m/s to 85 m/s. The findings are summarized as follows.

(1) Regarding the evaluation approach of HFFB, it is suggested to (a) envelope the responses across all angles of attack in the time and frequency domain results, and (b) use the cumulative largest structural responses up to a design wind speed to ensure a conservative MWFRS design.
(2) For SQ models, a larger SQ model can perform better than its counterpart under low wind speeds because of a higher resonant wind speed. Instead of applying an aerodynamic strategy, this characteristic can be leveraged to mitigate wind responses for cities with lower design wind speeds.
(3) For the cross-section modification models, the aerodynamic performance is influenced by both the PR (or DR) and WR. With the same PR, the ideal WRs are not on the boundaries (i.e., 0% or 100%) of the design space, which provides more flexibility for designers to pursue other objectives beyond aerodynamic responses.
(4) The downside of the subtractive-based corner recession strategy under low wind speeds is demonstrated through various models. Overall, the additive-based side protrusion strategy (if possible) has a higher chance to mitigate aerodynamic responses under a broad range of wind speeds than that of the subtractive-based corner recession strategy from the perspective of the same benchmark model, which provides useful information for the industry to apply cross-section modification for tall buildings.
(5) For the additive-based side protrusion strategy, promising aerodynamic performance can be achieved via various PRs. SP-7-86, SP-14-71, and SP-21-29 are the ideal candidates for minor, medium, and major protrusion strategies to suppress OTM over wind speeds of 35 m/s to 85 m/s. In comparison with SQ70, the OTM responses at the wind speeds of 53 m/s for the three models are reduced by 35%, 50%, and 48%, respectively.

The conclusions drawn above are based on HFFB testing, which is a useful and practical wind tunnel testing technique to understand the effects of external shapes on structural responses (displacement, acceleration, and OTM) for tall buildings. In the future, various wind tunnel testing techniques, such as simultaneous pressure measurement and particle image velocimetry, or CFD simulations, could be involved to delve deeper into the mechanism, including flow separation/attachment and wake effect, behind the structural responses presented.

CRediT authorship contribution statement

Wei-Ting Lu: Writing – review & editing, Writing – original draft, Visualization, Validation, Methodology, Investigation, Formal analysis, Data curation, Conceptualization. **Brian M. Phillips:** Writing – review & editing, Supervision, Resources, Project administration, Methodology, Funding acquisition, Conceptualization. **Zhaoshuo Jiang:** Writing – review & editing, Funding acquisition, Conceptualization.

Declaration of competing interest

The authors declare that they have no known competing financial interests or personal relationships that could have appeared to influence the work reported in this paper.

Data availability

Data will be made available on request.

Acknowledgments

This material is based upon work supported by the National Science Foundation (NSF) under Grants No. 2028762 & 2028647. Any opinions, findings, and conclusions or recommendations expressed in this material are those of the authors and do not necessarily reflect the views of NSF. The authors also acknowledge the NSF NHERI awardee that contributed to the research results reported within this paper under Grant No. 2037725: Natural Hazards Engineering Research Infrastructure: Experimental Facility with Boundary Layer Wind Tunnel 2021–2025 and Grant No. 2022469: Natural Hazards Engineering Research Infrastructure: Cyberinfrastructure (DesignSafe) 2020–2025.

References

Alminhana, G.W., Braun, A.L., Loredo-Souza, A.M., 2018. A numerical-experimental investigation on the aerodynamic performance of CAARC building models with geometric modifications. J. Wind Eng. Ind. Aerod. 180, 34–48.
ASCE 49-21, 2021. Wind Tunnel Testing for Buildings and Other Structures. American Society of Civil Engineers, Reston, VA.

ASCE 7-22, 2022. Minimum Design Loads and Associated Criteria for Buildings and Other Structures. American Society of Civil Engineers, Reston, VA.
ASCE, 2019. Prestandard for Performance-Based Wind Design. American Society of Civil Engineers, Reston, VA.
Bernardini, E., Spence, S.M.J., Wei, D., Kareem, A., 2015. Aerodynamic shape optimization of civil structures: a CFD-enabled Kriging-based approach. J. Wind Eng. Ind. Aerod. 144, 154–164.
Cao, Y., Tamura, T., 2018. Aerodynamic characteristics of a rounded-corner square cylinder in shear flow at subcritical and supercritical Reynolds numbers. J. Fluid Struct. 82, 473–491.
Carassale, L., Freda, A., Marre-Brunenghi, M., 2014. Experimental investigation on the aerodynamic behavior of square cylinders with rounded corners. J. Fluid Struct. 44, 195–204.
Catarelli, R.A., Fernández-Cabán, P.L., Masters, F.J., Bridge, J.A., Gurley, K.R., Matyas, C.J., 2020a. Automated terrain generation for precise atmospheric boundary layer simulation in the wind tunnel. J. Wind Eng. Ind. Aerod. 207, 104276.
Catarelli, R.A., Fernández-Cabán, P.L., Phillips, B.M., Bridge, J.A., Masters, F.J., Gurley, K.R., Prevatt, D.O., 2020b. Automation and new capabilities in the University of Florida NHERI boundary layer wind tunnel. Front. Built. Environ. 6.
Ding, F., Kareem, A., 2018. A multi-fidelity shape optimization via surrogate modeling for civil structures. J. Wind Eng. Ind. Aerod. 178, 49–56.
Ding, F., Kareem, A., 2020. Tall buildings with dynamic facade under winds. Engineering 6 (12), 1443–1453.
Dong, H., Chen, L., Du, X., Fang, L., Jin, X., 2022. Effects of corner chamfers on the extreme pressures on a square cylinder at incidence to a uniform flow. Comput. Fluid 244, 105539.
Ellis, B.R., 1980. As assessment of the accuracy of predicting the fundamental natural frequencies of buildings and the implications concerning the dynamic analysis of structures. Proc. Inst. Civ. Eng. 2 (69), 763–776. Sept.
Elshaer, A., Bitsuamlak, G., Damatty, A.E., 2017. Enhancing wind performance of tall buildings using corner aerodynamic optimization. Eng. Struct. 136, 133–148.
Elshaer, A., Bitsuamlak, G., 2018. Multiobjective aerodynamic optimization of tall building openings for wind-induced load reduction. J. Struct. Eng. 144 (10), 04018198.
Griffis, L.G., 1993. Serviceability limit states under wind load. Eng. J. AISC. 1st Qtr 1–16.
Gu, M., Quan, Y., 2004. Across-wind loads of typical tall buildings. J. Wind Eng. Ind. Aerod. 92 (13), 1147–1165.
Hou, F., Sarkar, P., Alipour, A., 2023. A novel mechanism - smart morphing façade system - to mitigate wind-induced vibration of tall buildings. Eng. Struct. 275, 115152.
Hu, G., Hassanli, S., Kwok, K.C.S., Tse, K.T., 2017. Wind-induced responses of a tall building with a double-skin façade system. J. Wind Eng. Ind. Aerod. 168, 91–100.
Hu, G., Song, J., Hassanli, S., Ong, R., Kwok, K.C.S., 2019. The effects of a double-skin façade on the cladding pressure around a tall building. J. Wind Eng. Ind. Aerod. 191, 239–251.
Hui, Y., Liu, J., Wang, J., Yang, Q., 2022. Effects of facade rib arrangement on aerodynamic characteristics and flow structure of a square cylinder. Build. Environ. 214, 108924.
Irwin, P.A., 2009. Wind engineering challenges of the new generation of super-tall buildings. J. Wind Eng. Ind. Aerod. 97 (7–8), 328–334.
Jafari, M., Alipour, A., 2021. Methodologies to mitigate wind-induced vibration of tall buildings: a state-of-the-art review. J. Build. Eng. 33, 101582.
Kawai, H., 1998. Effect of corner modifications on aeroelastic instabilities of tall buildings. J. Wind Eng. Ind. Aerod. 74–76, 719–729.
Kwok, K.C.S., Wilhelm, P.A., Wilkie, B.G., 1988. Effect of edge configuration on wind-induced responses of tall buildings. Eng. Struct. 10 (2), 135–140.
Kwon, D.K., Kijewski, T., Kareem, A., 2008. E-analysis of high-rise buildings subjected to wind loads. J. Struct. Eng. 134 (7), 1139–1153.
Li, Y., Li, C., Li, Q.S., Song, Q., Huang, X., Li, Y.G., 2020. Aerodynamic performance of CAARC standard tall building model by various corner chamfers. J. Wind Eng. Ind. Aerod. 202, 104197.
Li, Y., Tian, X., Tee, K.F., Li, Q.S., Li, Y.G., 2018. Aerodynamic treatments for reduction of wind loads on high-rise buildings. J. Wind Eng. Ind. Aerod. 172, 107–115.
Liu, J., Hui, Y., Wang, J., Yang, Q., 2021. LES study of windward-face-mounted-ribs' effects on flow fields and aerodynamic forces on a square cylinder. Build. Environ. 200, 107950.
Liu, J., Hui, Y., Yang, Q., Wang, J., 2023a. Numerical study of impact of façade ribs on the wind field and wind force of high-rise building under atmospheric boundary layer flow. J. Wind Eng. Ind. Aerod. 236, 105399.
Liu, J., Hui, Y., Yang, Q., Zhang, R., 2023b. LES evaluation of the aerodynamic characteristics of high-rise building with horizontal ribs under atmospheric boundary layer flow. J. Build. Eng. 71, 106487.
Liu, Z., Zheng, C., Wu, Y., Flay, R.G.J., Zhang, K., 2019. Investigation on the effects of twisted wind flow on the wind loads on a square section megatall building. J. Wind Eng. Ind. Aerod. 191, 127–142.
Lu, W.T., Phillips, B.M., Jiang, Z., 2023. Effects of side and corner modification on the aerodynamic behavior of high-rise buildings considering serviceability and survivability. J. Wind Eng. Ind. Aerod. 233, 105324.
Lu, W.T., Phillips, B.M., Jiang, Z., 2023b. Surrogate-based cyber-physical aerodynamic shape optimization of high-rise buildings using wind tunnel testing. J. Wind Eng. Ind. Aerod. 242, 105586.
Miyashita, K., Katagiri, J., Nakamura, O., Ohkuma, T., Tamura, Y., Itoh, M., Mimachi, T., 1993. Wind-induced response of high-rise buildings: effects of corner cuts or openings in square buildings. J. Wind Eng. Ind. Aerod. 50, 319–328.
Mooneghi, M.A., Kargarmoakhar, R., 2016. Aerodynamic mitigation and shape optimization of buildings: review. J. Build. Eng. 6, 225–235.
Moorjani, R.R., Lombardo, F.T., Devin, A.F., Young, B.S., Baker, W.F., Ray, S.D., 2021. Influence of vented floors on the across-wind response of tall buildings. J. Wind Eng. Ind. Aerod. 209, 104480.
Paul, R., Dalui, S.K., 2021. Optimization of alongwind and crosswind force coefficients on a tall building with horizontal limbs using surrogate modeling. Struct. Des. Tall Special Build. 30 (4), e1830.
Quan, Y., Kuang, J., Gu, M., Wang, S., 2016. Effects of grid curtains on the wind loads of a high-rise building. Struct. Des. Tall Special Build. 25, 245–262.
Sharma, A., Mittal, H., Gairola, A., 2018. Mitigation of wind load on tall buildings through aerodynamic modifications: review. J. Build. Eng. 18, 180–194.
Skvorc, P., Hozmar, H., 2023. The effect of wind characteristics on tall buildings with porous double-skin façades. J. Build. Eng. 69, 106135.
Stathopoulos, S., Zhu, X., 1990. Wind pressures on buildings with mullions. J. Struct. Eng. 116 (8), 2272–2291.
Tamura, T., Miyagi, T., 1999. The effect of turbulence on aerodynamic forces on a square cylinder with various corner shapes. J. Wind Eng. Ind. Aerod. 83, 135–145.
Tamura, Y., 2012. Amplitude dependency of damping in buildings and critical tip drift ratio. Int. J. High-Rise Build. 1 (1), 1–13.
Tanaka, H., Tamura, Y., Ohtake, K., Nakai, M., Kim, Y.C., 2012. Experimental investigation of aerodynamic forces and wind pressures acting on tall buildings with various unconventional configurations. J. Wind Eng. Ind. Aerod. 107–108, 179–191.
Tang, L., Zheng, C., Liu, H., 2023. Effects of corner-recession on wind-induced responses and aerodynamic damping of a square megatall building under twisted wind flow. J. Build. Eng. 75, 107018.
Thordal, M.S., Bennetsen, J.C., Capra, S., Kragh, A.K., Holger, H., Koss, H., 2020. Towards a standard CFD setup for wind load assessment of high-rise buildings: Part 2 – blind test of chamfered and rounded corner high-rise buildings. J. Wind Eng. Ind. Aerod. 205, 104282.
Tschanz, T., Davenport, A.G., 1983. The base balance technique for the determination of dynamic wind loads. J. Wind Eng. Ind. Aerod. 13 (1–3), 429–439.
Tse, K.T., Hitchcock, P.A., Kwok, K.C., Thepmongkorn, S., Chan, C.M., 2009. Economic perspectives of aerodynamic treatments of square tall buildings. J. Wind Eng. Ind. Aerod. 97 (9–10), 455–467.
Tse, K.T., Hu, G., Song, J., Park, H.S., Kim, B., 2021. Effects of corner modifications on wind loads and local pressures on walls of tall buildings. Build. Simulat. 14, 1109–1126.
Tse, K.T., Weerasuriya, A.U., Kwok, K.C.S., 2016. Simulation of twisted wind flows in a boundary layer wind tunnel for pedestrian-level wind tunnel tests. J. Wind Eng. Ind. Aerod. 159, 99–109.
Xie, J., 2014. Aerodynamic optimization of super-tall buildings and its effectiveness assessment. J. Wind Eng. Ind. Aerod. 130, 88–98.
Yan, B., Ding, W., Zhou, X., Guo, K., Ren, H., Li, X., Yang, Q., 2023. Experimental study on the aeroelastic response of a square supertall building considering twisted wind effect. Eng. Struct. 283, 115923.
Yuan, Y., Yan, B., Zhou, X., Yang, Q., Wei, M., He, Y., Zhou, X., Li, X., 2023. Twisted-wind effect on the aerodynamic force acting on varying side-ratios tall buildings. J. Wind Eng. Ind. Aerod. 240, 105481.
Zheng, C., Xie, Y., Khan, M., Wu, Y., Liu, J., 2018. Wind-induced responses of tall buildings under combined aerodynamic control. Eng. Struct. 175, 86–100.
Zhou, L., Hu, G., Tse, K.T., He, X., 2021. Twisted-wind effect on the flow field of tall building. J. Wind Eng. Ind. Aerod. 218, 104778.
Zhou, Y., Kijewski, T., Kareem, A., 2003. Aerodynamic loads on tall buildings: interactive database. J. Struct. Eng. 129 (3), 394–404.